



<http://www.diva-portal.org>

Postprint

This is the accepted version of a paper presented at *Workshop on Insight on Eye Biometrics, IEB, in conjunction with the 10th International Conference on Signal-Image Technology and Internet-Based Systems, SITIS 2014, Marrakech, Morocco, 23-27 November, 2014.*

Citation for the original published paper:

Alonso-Fernandez, F., Bigun, J. (2014)

Fake Iris Detection: A Comparison Between Near-Infrared and Visible Images.

In: Kokou Yetongnon, Albert Dipanda & Richard Chbeir (ed.), *Proceedings: 10th International Conference on Signal-Image Technology and Internet-Based Systems, SITIS 2014* (pp. 546-553).

Piscataway, NJ: IEEE Computer Society

<http://dx.doi.org/10.1109/SITIS.2014.104>

N.B. When citing this work, cite the original published paper.

Permanent link to this version:

<http://urn.kb.se/resolve?urn=urn:nbn:se:hh:diva-26870>



Fig. 2. Examples of real and fake images acquired with visible (top) and near-infrared (bottom) cameras.

by the system, and of those, more than 50% were matched successfully with its corresponding real sample. Also, as color contact lenses are becoming popular, another potential mean of spoofing is by using contact lenses with artificial textures. Wei *et al.* [7] presented a database of 640 fake images from people wearing contact lenses from two manufacturers with 20 different artificial textures. They also proposed three measures (edge sharpness, Iris-Texton and three features from the co-occurrence matrix) to detect the printed contact lenses, reaching classification rates in the range of 76% to 100% (depending on the measure and manufacturer). In previous studies, Daugman proposed the use of spurious energy in the Fourier spectrum to detect printed iris patterns [8]. Lee *et al.* suggested the Purkinje image to detect fake iris [9], while He *et al.* used four image features (mean, variance, contrast and angular second moment) for this purpose [10]. There has been also research concerned with the synthesis of artificial images [11], accompanied by the release of datasets, such as the WVU-Synthetic Iris DB². In 2013, LivDet-Iris 2013, the first Liveness Detection Iris Competition³, was organized. The datasets utilized included iris data from people wearing contact lenses and printouts of real iris images (with more than 4000 real and 3000 fake images). Classification rates averaged over the different types of data were in the range of 12%-25%. One difficulty of LivDet-Iris 2013 was the use of different contact lens manufacturers and different printers in the training and test data. Lastly, Galbally *et al.* proposed a general technique based on image quality features which allows detection of fake samples in image-based biometric modalities [3]. The latter followed a previous framework that we initiated with the use of trait-specific quality properties for liveness detection, including fingerprints [12], [13] and iris

²Available at www.citer.wvu.edu

³<http://people.clarkson.edu/projects/biosal/iris/index.php>

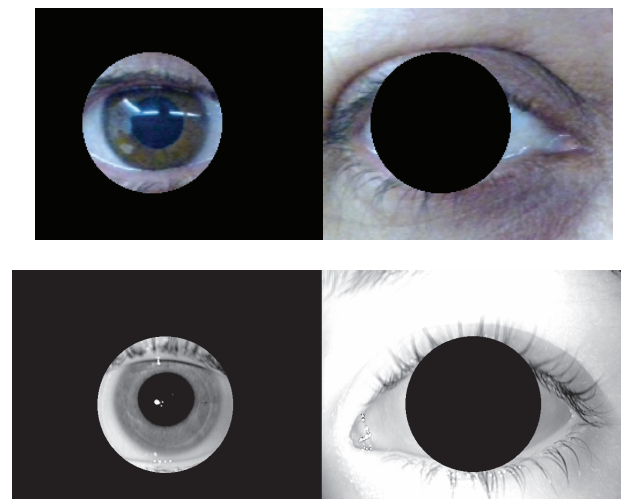


Fig. 3. Mask of surrounding periocular and eye region on visible (top) and near-infra-red (bottom) images.

[14]. For the case of iris samples, the experiments reported in [3] achieved a classification rate of over 97% using the ATVS-Flr DB, and nearly 90% using synthetic iris images from the WVU-Synthetic Iris DB.

The preferred choice of current commercial iris systems is near-infrared (NIR) sensors. As a result, all of the above-mentioned works have concentrated their efforts in data of this class. However, visible wavelength imaging with color information are more appropriate for newer applications based on distant acquisition and 'on the move' capabilities [15]. Recently, the MobBIOfake database [16] has been released in the framework of MobILive 2014, the 1st Mobile Iris Liveness Detection Competition⁴. Being among the first of its class, this is a dataset of 800 fake iris images (and its corresponding real images) acquired with a color webcam of a Tablet PC. In a previous preliminary work [17], we have evaluated the use of Gray-Level Co-Occurrence (GLCM) textural features [18], [19], [20] for the task of fake iris detection using such database. To the best of our knowledge, it has been the first work evaluating spoofing attacks using color images in the visible range. This paper complements our previous research, providing also comparative experiments with the ATVS-Flr DB captured in the NIR range (Figure 2) in which, we assume, is among the first papers in comparing the two types of data. The best GLCM features are selected by Sequential Forward Floating Selection (SFFS) [21], and the classification is performed using a linear SVM as classifier [22] (we do not use higher order kernels, since we found in our previous study [17] that they do not provide better classification results). We observe that, comparatively, fake images from the NIR sensor are easier to detect (with a correct classification rate of over 99.5%). An appropriate selection of features from the RGB color channels of visible images allows to achieve a correct classification rate of over 96%, but at

⁴<http://mobilive2014.inescporto.pt>

the expense of needing twice as much features than the NIR sensor. We also observe that downsampling the NIR images (to equate the average iris size between the two databases) has little impact in the classification accuracy. We also evaluate the extraction of GLCM features from the whole image vs. the extraction from selected (eye or periocular) regions only (Figure 3). A related study combining features from the iris and surrounding eye regions has been recently presented [23], although this study only used NIR data, and was not intended to assess which are the best regions for iris fake detection, but just to combine data from them. Our experiments show that extracting features from the iris texture region only is not the best option with either sensor, highlighting that both the eye region and the surrounding periocular (skin) region provide valuable information for fake image detection, regardless of the imaging conditions. This also provides another advantage in the sense that no accurate iris segmentation is needed, providing computational time savings and reduced complexity. These are desired properties, specially in real scenarios, where accurate iris segmentation may not be even possible [3].

II. GLCM TEXTURAL FEATURES

We employ the Gray Level Co-occurrence Matrix (GLCM) [18], [19], [20] for fake iris detection. The GLCM is a joint probability distribution function of gray level pairs in a given image $I(p, q)$. Each element $C(i, j)$ in the GLCM specifies the probability that a pixel with intensity value i occurs in the image $I(p, q)$ at an offset $d = (\Delta p, \Delta q)$ of a pixel with intensity value j . Usually the computation is done between neighboring pixels (i.e. $\Delta p = 1$ or $\Delta q = 1$). To achieve rotational invariance, the GLCM is computed using a set of offsets uniformly covering the 0-180 degrees range (e.g. 0, 45, 90 and 135 degrees). Once the GLCM is computed, various texture features are extracted and averaged across the different orientations. Let P_{ij} be the (i, j) entry in the GLCM. The features extracted are as follows:

$$\text{Contrast: } f_1 = \sum_{i,j=0}^{N-1} P_{ij} (i - j)^2$$

$$\text{Dissimilarity: } f_2 = \sum_{i,j=0}^{N-1} P_{ij} |i - j|$$

$$\text{Homogeneity: } f_3 = \sum_{i,j=0}^{N-1} \frac{P_{ij}}{1 + |i - j|}$$

$$\text{Inverse Difference Moment: } f_4 = \sum_{i,j=0}^{N-1} \frac{P_{ij}}{1 + (i - j)^2}$$

$$\text{Energy: } f_5 = \sum_{i,j=0}^{N-1} P_{ij}^2$$

$$\text{Maximum Probability: } f_6 = \max_{i,j} P_{ij}$$

$$\text{Entropy: } f_7 = \sum_{i,j=0}^{N-1} P_{ij} (-\ln P_{ij})$$

$$\text{GLCM mean: } f_8 = \mu_i = \sum_{i,j=0}^{N-1} i P_{ij}$$

$$\text{GLCM std: } f_9 = \sigma_i = \sqrt{\sum_{i,j=0}^{N-1} P_{ij} (i - \mu_i)^2}$$

$$\text{GLCM Autocorrelation: } f_{10} = \sum_{i,j=0}^{N-1} ij P_{ij}$$

$$\text{GLCM correlation: } f_{11} = \sum_{i,j=0}^{N-1} P_{ij} \frac{(i - \mu_i)(j - \mu_j)}{\sigma_i \sigma_j}$$

$$\text{Cluster shade: } f_{12} = \sum_{i,j=0}^{N-1} P_{ij} ((i - \mu_i) + (j - \mu_j))^3$$

$$\text{Cluster prominence: } f_{13} = \sum_{i,j=0}^{N-1} P_{ij} ((i - \mu_i) + (j - \mu_j))^4$$

In computing f_{11} , f_{12} and f_{13} , it must be considered that $\mu_i = \mu_j$ and $\sigma_i = \sigma_j$, due to the symmetry property of the GLCM [18]. Features f_1 to f_4 are related to contrast of the image, using weights related to the distance to the GLCM diagonal. Values of the diagonal show no contrast (pixel pairs with equal gray level), with contrast increasing away from the diagonal. Features f_5 to f_7 measure the regularity or order of the pixels in the image. Weights here are constructed based on how many times a pixel pair occur (given by P_{ij}). Lastly, features f_8 to f_{13} consist of statistics derived from the GLCM. All the extracted features are grouped into a single vector, which is used to model the image. We then use a linear SVM as classifier [22]. We do not use higher order kernels, since we found [17] that they do not provide better classification results.

III. DATABASE AND PROTOCOL

For our experiments, we use the ATVS-Flr [6] and the MobBIOfake [16] databases. Both databases consist of a set of real images, and the corresponding fake samples obtained from printed images of the original ones, which are then captured with the same sensor. We use the training dataset of MobBIOfake, which contains 400 iris images from 50 volunteers, and their corresponding fake copies. Samples were acquired with an Asus Eee Pad Transformer TE300T Tablet. The size of the color (RGB) iris images is of 200×240 pixels (height \times width). Each volunteer contributed with 4 images of the two eyes. ATVS-Flr has 800 real (and their corresponding fake images) from 50 subjects, with each subject providing 4 images of the 2 eyes in 2 different sessions. Samples were acquired with the LG IrisAccess EOU3000 sensor with NIR illumination, which captures grey-scale images of 480×640 pixels. To avoid biased results in comparative experiments due to using a bigger number of NIR samples for training and testing, here we use only 400 real (and the corresponding fake samples) from ATVS-Flr.

The task of fake biometric detection can be modeled as a two-class classification problem. The metrics to evaluate the classification accuracy are: *False Acceptance Rate* (FAR), percentage of fake samples classified as real, and *False Rejection Rate* (FRR), percentage of real samples classified as fake. The average classification error (*Half Total Error Rate*) is then computed as $\text{HTER} = (\text{FAR} + \text{FRR})/2$. Classification accuracy has been measured by cross-validation [24]. Each database is divided into three disjoint sets, each set comprising one third of the available real images and their corresponding fake images. Two sets are chosen for training the classifier and one for testing, repeating the selection to consider the different possibilities. This yields to three classification errors, which are then averaged. We also evaluate different combinations of GLCM features for classification using SVMs. The best

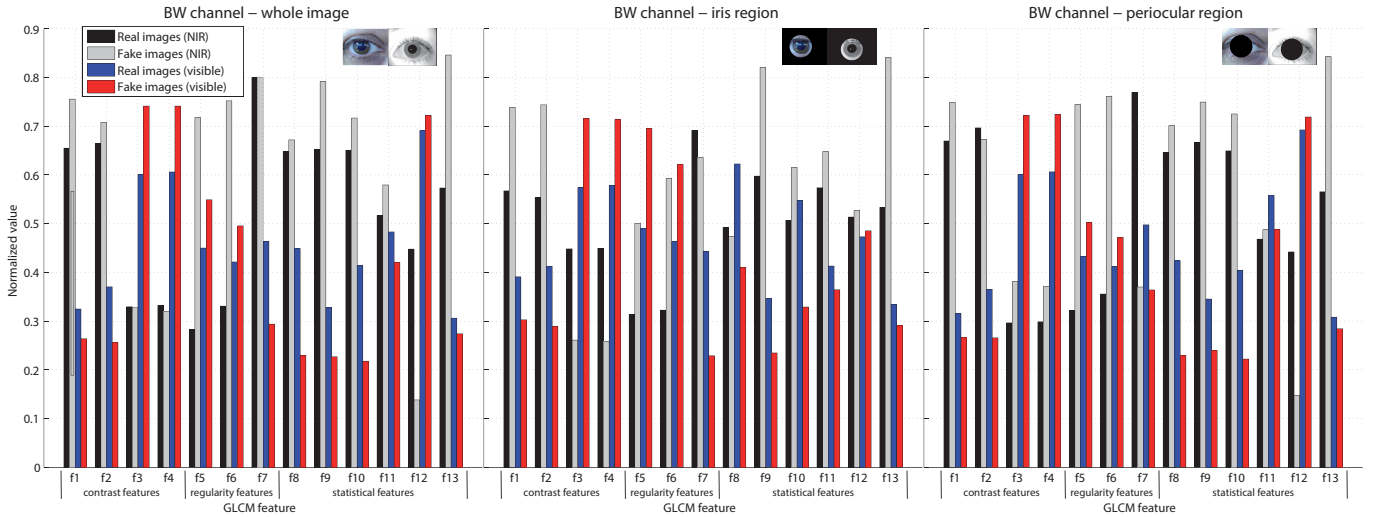


Fig. 4. Histogram of GLCM features for real and fake images (averaged over all available images of each class and normalized to the 0-1 range). Left: GLCM extracted from the whole image. Middle: GLCM extracted from the iris texture region. Right: GLCM extracted from the surrounding (periocular) region. For further details of the different regions considered, see Figure 3.

combination is found by Sequential Forward Floating Selection (SFFS) [21]. Given n features to combine, we employ as criterion value the HTER of the corresponding classifier trained with the n features.

We also conduct detection experiments to localize the eye center position, which is used as input to extract GLCM features in the relevant eye/periocular region only. We employ our eye detection algorithm based on symmetry filters described in [25]. A circular mask of fixed radius is placed in the eye center, masking the corresponding outer (periocular) or inner (eye) region, depending on the experiment at hand (Figure 3). The radius has been chosen empirically, based on the maximum radius of the outer (sclera) iris circle obtained by ground-truth annotation of the databases [26].

IV. RESULTS

Figure 4 shows the distribution of GLCM features on the real and fake iris images of the two databases (averaged between all images of each class and normalized to the [0,1] range). Normalization is done by considering all images of the two databases together, thus we can observe relative intra- and inter-database behaviors. GLCM features of the visible database are extracted from the luminance (BW) channel, to allow comparison with the NIR database. We evaluate three different cases in our experiments: *i*) GLCM features are extracted from the whole image, *ii*) GLCM features are extracted from the eye (iris) region only, and *iii*) GLCM features are extracted from the surrounding periocular region only. It can be observed that GLCM features have generally a different range for each database (for example, f1 has higher values with NIR images than with visible images). In addition, the relative inter-class variation is different for each database (following with f1, fake NIR images have higher values than real NIR images, but the opposite happens with the visible database). With respect to the three different regions

defined for feature extraction, all contrast features (f1 to f4) have a similar inter-database behavior in the three cases. On the contrary, the regularity features (f5 to f7) have different behavior depending on the region of analysis. Of particular interest is f11, which has a similar range for the two databases and the two classes in the left and right plots of Figure 4, but has a clear different range for each database when computed in the iris region only (center plot). A similar phenomenon can be observed with f12.

Classification results of each individual GLCM feature are given in Figure 5 (HTER values). We give results of features extracted from the luminance (BW) channel in the top row. Given the different image size of the two databases, we introduce an additional case with the NIR database for the sake of comparison: images are downsampled by 1/3, so as to have the circles of the iris boundaries with the same average size than the visible database (this downsampling factor is obtained empirically based on the available groundtruth annotation of the two databases [26]). For the visible sensor, we also provide results with features extracted separately from the R, G and B channels separately (bottom row). In addition, classification results of different combinations of GLCM features as selected with SFFS are given in Figure 6. SFFS experiments are first run on the luminance channel of the image, with 13 available features (columns 1-3). For the visible sensor, we also run SFFS by pooling together the R, G and B features, having in this case $13 \times 3 = 39$ features available for selection (column 4).

From Figure 5, we observe that the behavior of the individual features is different depending on the sensor. With the visible sensor, GLCM features work better in the iris region (blue curve), with the best features consistently being f7, f9, f13 and f1-f5 (the latter depending on the channel used). It is remarkable that GLCM features perform best when they are extracted from the R channel, with the best HTER in the range

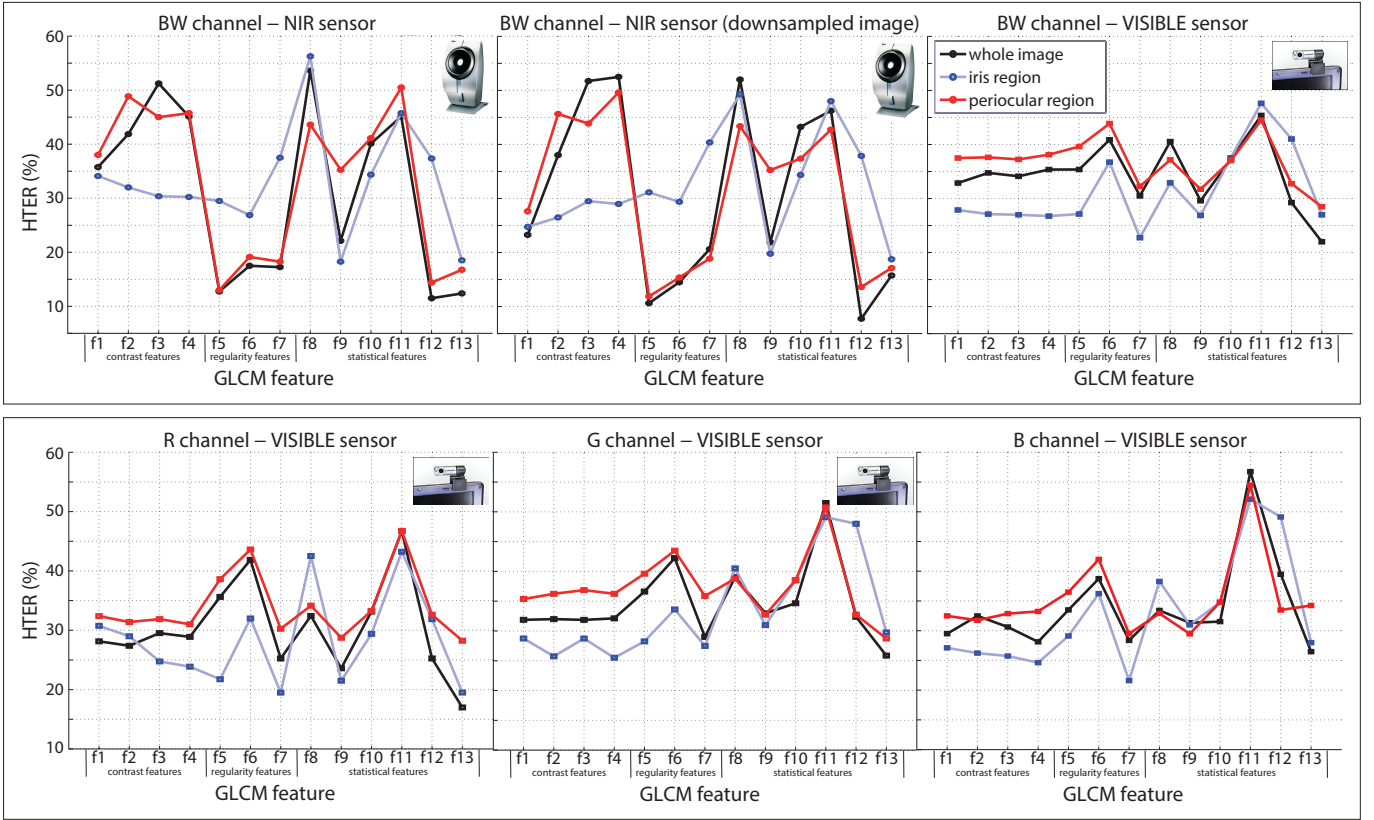


Fig. 5. Individual performance of GLCM features in the different regions considered (see Figure 3). Top row: GLCM extracted from the gray channel. Bottom row: GLCM extracted from the RGB channels (sensor with visible light only).

of 20 to 25%. On the other hand, with the NIR sensor, GLCM features work better when extracted from the periocular region (red curve) or from the whole image (black curve). The best features in these cases are f5-f7 and f12-f13, with HTER ranging from 10 to 20%, which is lower than the best HTER achieved with the visible sensor. Downsampling NIR images does not have a significant impact in the performance of the best features either (some features even perform better with downsampled images, such as f1 or f2).

Concerning the combination of GLCM features by SFFS, we observe (Figure 6) that a substantial performance improvement can be obtained in most cases with an appropriate combination of features. With the visible sensor, the improvement is not so evident if only the luminance information is used (third column). This can be overcome by selecting features from the three RGB channels (fourth column), meaning that the color information contribute to the success of fake iris detection in this imaging conditions. In addition, no significant decrease in performance is observed with the NIR sensor after image downsampling (second vs. first column). We give in Tables I and II the features chosen by SFFS at the minimum HTER value for all cases of Figure 6 (except for the second column). For the NIR sensor, the best performance can be obtained by combining a small number of features (5 to 7), but the visible sensor requires approximately twice as much (12 features) to achieve the minimum classification error.

Considering the three different regions defined for feature extraction, the best classification rate with the visible sensor is obtained when GLCM features from the whole image are used (top right, Figure 6), with a minimum HTER of less than 4%. An added advantage of this result is that no iris detection or segmentation is needed. This is in contrast with Figure 5, where we observed that GLCM features work better individually with this sensor if they are extracted not from the whole image, but from the iris region only. Selected features (Table II) are equally chosen from the three color channels (4 from each one), with a tendency towards choosing features from the ‘statistics’ class (f8 to f13, with 8 features selected) and very few from the ‘contrast’ class (f1 to f4, with only one feature selected). For the other two regions of analysis, the lowest classification error with appropriate feature selection is in the range of 6-7%. Also here there is a tendency towards not considering features from the ‘contrast’ class.

With the NIR sensor, the best classification rate is obtained with GLCM features from the periocular region, although using features from the whole image also provides a good accuracy (above 99.5%). This is in tune with the behavior of the individual features observed above (Figure 5). Selected features in these two cases (Table I) also include the ‘statistics’ class to a great extent, but the preferred features are different. For example, f13 is never selected with the NIR sensor, but it is selected from two RGB channels of the visible sensor.

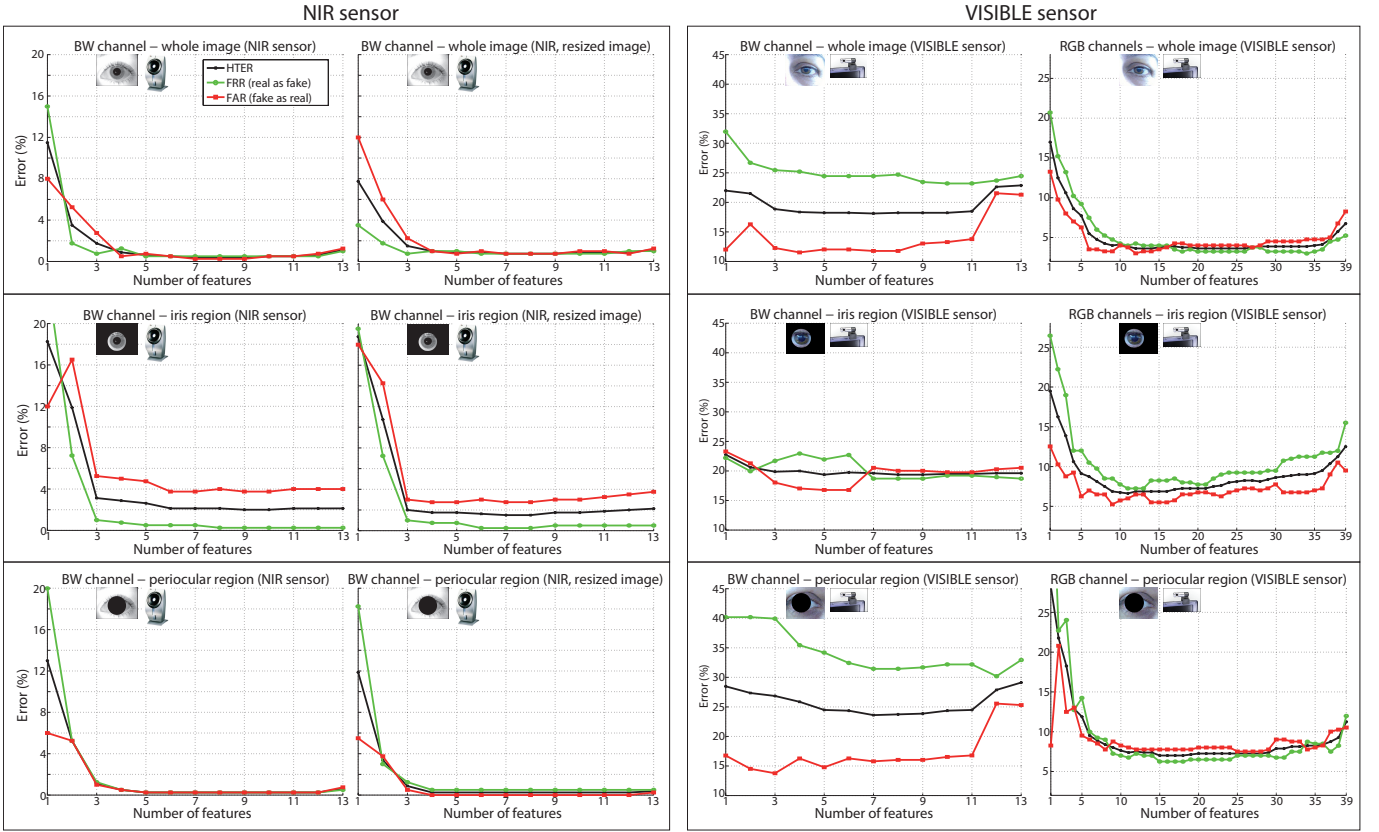


Fig. 6. Classification results (FAR, FRR and HTER) for an increasing number of textural features (selected with SFFS). Left: GLCM extracted from the whole image. Middle: GLCM extracted from the iris texture region. Right: GLCM extracted from the surrounding (periocular) region. For further details of the different regions considered, see Figure 3. For each case (row), four cases are depicted: gray scale images from the NIR sensor (column 1), gray scale images from the NIR sensor with image downsampling (column 2), gray scale images from the webcam (visible) sensor (column 3), color images from the webcam (visible) sensor (column 4).

Similarly, feature f9 is not selected with the NIR sensor in the optimal case (periocular), but it is selected from the three RGB channels of the visible sensor. The preference for each type of ‘statistics’ features is even more evident if we compare the features selected from the luminance channel only by each sensor (top and bottom of Table I). In addition, the NIR sensor shows a higher tendency towards choosing ‘contrast’ features.

What it is clear from our experiments is that extracting features only from the iris texture region provides worse accuracy with either sensor. An added undesirable effect in this latter case is that the difference between FRR and FAR tends to increase (second row of Figure 6). We also observe with the NIR sensor that the FAR (red curves) is higher than the FRR (green curves), meaning that the system has tendency towards accepting fake images as real. The opposite is observed with the visible sensor, implying a higher tendency towards misclassifying a real image.

V. CONCLUSIONS

Previous research on fake iris detection has concentrated their efforts in data acquired with near-infrared (NIR) sensors (providing gray-scale images), which is the preferred choice of current commercial imaging systems [15]. In a previous work

[17], we addressed the task of fake iris detection using visible images [17]. This paper complements our previous work with new and extended experiments, providing comparison with data captured in the NIR range. This is, to the best of our knowledge, among the first works in evaluating fake iris data in visible range and providing comparative experiments between the two types of data. Fake samples in our experiments are obtained from printed images, which are presented to the same sensor than the real ones. We employ GLCM textural features [18], [19], [20] and SVM classifiers [22] for the task of fake iris detection, with the best features selected via SFFS [21]. GLCM features analyze various image properties related with contrast, pixel regularity, as well as pixel co-occurrence statistics. Comparatively, fake images from the NIR sensor are easier to detect (correct classification rate of over 99.5%). While the visible sensor achieves a classification rate of only 82% when features are extracted from the luminance channel, it can go up to 96% if features are selected from the three RGB color channels simultaneously. The latter, however, comes at the expense of needing twice as much features to achieve the maximum classification rate (12 with the visible sensor vs. 5 with the NIR sensor). Also, additional downsampling of NIR images by a factor of 3 (to equate the average size of the iris

		NIR sensor (BW channel)															
region	#	f1	f2	f3	f4	f5	f6	f7	f8	f9	f10	f11	f12	f13	htr	frr	far
whole	7	x		x	x	x			x	x	x				0.38	0.5	0.25
eye	6	x		x	x			x			x		x		2.13	0.5	3.75
periocular	5			x				x	x		x			x	0.25	0.25	0.25
		contrast			regul.			statistics									

		VISIBLE sensor (BW channel)															
region	#	f1	f2	f3	f4	f5	f6	f7	f8	f9	f10	f11	f12	f13	htr	frr	far
whole	5	x		x				x					x	x	18.24	24.45	12.03
eye	5								x			x	x	x	19.37	21.96	16.79
periocular	7			x	x			x	x			x	x	x	23.61	31.44	15.78
		contrast			regul.			statistics									

TABLE I

FEATURES SELECTED BY SFFS FOR DIFFERENT EXTRACTION REGIONS (SFFS APPLIED TO GLCM FEATURES FROM THE LUMINANCE CHANNEL).

		R channel													G channel													B channel															
region	#	f1	f2	f3	f4	f5	f6	f7	f8	f9	f10	f11	f12	f13	f1	f2	f3	f4	f5	f6	f7	f8	f9	f10	f11	f12	f13	f1	f2	f3	f4	f5	f6	f7	f8	f9	f10	f11	f12	f13	htr	frr	far
whole	12						x		x	x			x					x					x											x	x	x				3.62	4.24	3.01	
iris	11				x		x	x					x	x				x					x											x						6.62	7.25	5.99	
perioc	15						x	x		x	x	x	x	x	x		x						x	x	x			x							x	x					7.01	6.25	7.76
		contrast			regul.			statistics			contrast			regul.			statistics			contrast			regul.			statistics																	

TABLE II

FEATURES SELECTED BY SFFS FOR DIFFERENT EXTRACTION REGIONS (VISIBLE SENSOR, SFFS APPLIED TO GLCM FEATURES FROM THE THREE RGB CHANNELS TOGETHER).

region between the two databases) shows little impact in the classification accuracy.

We also analyze the extraction of GLCM features from the whole image vs. the extraction from selected (eye or periocular) regions only. Maximum accuracy can be obtained when features are extracted from the whole image, pointing out that both the eye and the surrounding periocular region contribute to the success of the fake detection task for the two imaging conditions studied. An added advantage is that no accurate iris segmentation is needed. Further analysis reveals that both sensors tend to choose GLCM features measuring statistical properties of the image, but the selected features are different for each case. In addition, the NIR sensor shows higher tendency towards choosing GLCM contrast features, which are hardly selected with the visible sensor.

Currently, we are working towards including other type of fake data in our analysis, such as contact lenses [7]. Another source of future work is the evaluation of other features already proposed for fake iris detection, e.g. [3]. We are also working on combining features from different regions of the image [23], instead of restricting the SFFS selection to features extracted from one region only.

ACKNOWLEDGMENT

Author F. A.-F. thanks the Swedish Research Council and the EU for funding his postdoctoral research. Authors acknowledge the CAISR program of the Swedish Knowledge Foundation and the EU COST Action IC1106. Authors also thank the Biometric Recognition Group (ATVS-UAM) for making the ATVS-Flr database available.

REFERENCES

- [1] B. Schneier, "The uses and abuses of biometrics," *Communications of the ACM*, vol. 48, p. 136, 1999.
- [2] N. Ratha, J. Connell, and R. Bolle, "An analysis of minutiae matching strength," *Proc. International Conference on Audio- and Video-Based Biometric Person Authentication, AVBPA*, vol. Springer LNCS-2091, pp. 223–228, 2001.
- [3] J. Galbally, S. Marcel, and J. Fierrez, "Image quality assessment for fake biometric detection: Application to iris, fingerprint, and face recognition," *IEEE Transactions on Image Processing*, vol. 23, no. 2, pp. 710–724, Feb 2014.
- [4] K. Bowyer, K. Hollingsworth, and P. Flynn, "Image understanding for iris biometrics: a survey," *Computer Vision and Image Understanding*, vol. 110, pp. 281–307, 2007.
- [5] D. Monro, S. Rakshit, and D. Zhang, "DCT-Based iris recognition," *IEEE Trans. on Pattern Analysis and Machine Intelligence*, vol. 29, no. 4, pp. 586–595, April 2007.
- [6] V. Ruiz-Albacete, P. Tome-Gonzalez, F. Alonso-Fernandez, J. Galbally, J. Fierrez, and J. Ortega-Garcia, "Direct attacks using fake images in iris verification," *Proc. COST 2101 Workshop on Biometrics and Identity Management, BIOD*, vol. Springer LNCS-5372, pp. 181–190, 2008.
- [7] Z. Wei, X. Qiu, Z. Sun, and T. Tan, "Counterfeit iris detection based on texture analysis," *Proc. 19th International Conference on Pattern Recognition, ICPR*, pp. 1–4, 2008.
- [8] J. Daugman, "Demodulation by complex-valued wavelets for stochastic pattern recognition," *International Journal of Wavelets, Multi-resolution and Information Processing*, vol. 1, pp. 1–17, 2003.
- [9] E. C. Lee, K. R. Park, and J. Kim, "Fake iris detection by using purkinje image," *Proc. International Conference in Biometrics, ICB*, vol. Springer LNCS-3832, pp. 397–403, 2006.
- [10] X. He, S. An, and P. Shi, "Statistical texture analysis-based approach for fake iris detection using support vector machines," *Proc. International Conference on Biometrics, ICB*, vol. Springer LNCS-4642, pp. 540–546, 2007.
- [11] S. Shah and A. Ross, "Generating synthetic irises by feature agglomeration," in *Proc. IEEE International Conference on Image Processing, ICIP*, Oct 2006, pp. 317–320.
- [12] J. Galbally, F. Alonso-Fernandez, J. Fierrez, and J. Ortega-Garcia, "A high performance fingerprint liveness detection method based on quality related features," *Elsevier Future Generation Computer Systems Journal*, vol. 28, no. 1, pp. 311–321, 2012.

- [13] J. Galbally, F. Alonso-Fernandez, J. Fierrez-Aguilar, and J. Ortega-Garcia, "Fingerprint Liveness Detection Based on Quality Measures," *Proc. IEEE Intl. Conf. on Biometrics, Identity and Security, BIDS*, 2009.
- [14] J. Galbally, J. Ortiz-Lopez, J. Fierrez, and J. Ortega-Garcia, "Iris liveness detection based on quality related features," in *Proc. 5th IAPR International Conference on Biometrics, ICB*, March 2012, pp. 271–276.
- [15] K. W. Bowyer, K. P. Hollingsworth, and P. J. Flynn, "A survey of iris biometrics research: 2008-2010," in *Handbook of Iris Recognition*, ser. Advances in Computer Vision and Pattern Recognition, M. J. Burge and K. W. Bowyer, Eds. Springer London, 2013, pp. 15–54.
- [16] A. F. Sequeira, J. Murari, and S. Cardoso, "Iris liveness detection methods in mobile applications," *Proc International Conference on Computer Vision Theory and Applications, VISAPP*, 2014.
- [17] F. Alonso-Fernandez and J. Bigun, "Exploiting periocular and RGB information in fake iris detection," *Proc. 37th International Convention on Information and Communication Technology, Electronics and Microelectronics, MIPRO, Special Session on Biometrics, Forensics, De-identification and Privacy Protection, BiForD, Opatija, Croatia*, 2014.
- [18] R. Haralick, K. Shanmugam, and I. Dinstein, "Textural features for image classification," *IEEE Trans. on Systems, Man and Cybernetics*, vol. SMC-3, no. 6, pp. 610–621, Nov 1973.
- [19] L.-K. Soh and C. Tsatsoulis, "Texture analysis of sar sea ice imagery using gray level co-occurrence matrices," *IEEE Trans. on Geoscience and Remote Sensing*, vol. 37, no. 2, pp. 780–795, Mar 1999.
- [20] D. A. Clausi, "An analysis of co-occurrence texture statistics as a function of grey level quantization," *Canadian Journal of Remote Sensing*, vol. 28, no. 1, pp. 45–62, 2002.
- [21] P. Pudil, J. Novovicova, and J. Kittler, "Flotating search methods in feature selection," *Pattern Recognition Letters*, vol. 15, pp. 1119–1125, 1994.
- [22] V. N. Vapnik, *The Nature of Statistical Learning Theory*. New York, NY, USA: Springer-Verlag New York, Inc., 1995.
- [23] C. W. Tan and A. Kumar, "Integrating ocular and iris descriptors for fake iris image detection," *Proc. 2nd International Workshop on Biometrics and Forensics, IWBF, Valletta, Malta*, 2014.
- [24] R. Duda, P. Hart, and D. Stork, *Pattern Classification - 2nd Edition*, 2004.
- [25] F. Alonso-Fernandez and J. Bigun, "Eye detection by complex filtering for periocular recognition," *Proc. 2nd International Workshop on Biometrics and Forensics, IWBF, Valletta, Malta*, 2014.
- [26] H. Hofbauer, F. Alonso-Fernandez, P. Wild, J. Bigun, and A. Uhl, "A ground truth for iris segmentation," *Proc. International Conference on Pattern Recognition, ICPR*, 2014.